NATURAL SCIENCE REVIEW 2 100303 (2025)
nsr.jinr.int

Characterization of micro-SPECT system based on Timepix detector

V. Rozhkov*[1], I. Hernández[1,2], A. Leyva[3], and A. Zhemchugov[1]

[1] *Joint Institute for Nuclear Research, Dubna, Russia*
[2] *Isotopes Center, Mayabeque, Cuba*
[3] *Center of Technological Applications and Nuclear Development, Havana, Cuba*

Abstract

In this work, the characteristics of a prototype SPECT system based on the Timepix readout chip, with a MURA-type encoding mask, were evaluated. The setup has a small FoV and can be used in preclinical studies of drugs on small laboratory animals. Despite many existing test protocols developed and described in pertinent documents of national standard bodies and IAEA recommendations, they are not suitable for microtomographic systems based on semiconductor pixel detectors due to different detector technology, high spatial resolution and small area of interest. To measure their characteristics, special phantoms were developed, with a small "hot region".

Such micro-SPECT parameters as spatial resolution, contrast, linearity, and system efficiency were studied using ^{99m}Tc source. The detector calibration and data preprocessing are described.

Keywords: coded aperture, Timepix, SPECT

DOI: 10.54546/NaturalSciRev.100303

1. Introduction

In recent years, the use of radiotracers has found a wide application in diagnostic medicine and preclinical drug testing, where information about the dynamics of labeled molecule accumulation is obtained. In such molecules, some stable atoms are replaced by radioactive ones that are chemically equivalent. By binding these compounds to specific proteins, it is possible to deliver them to targeted organs. Depending on the isotope decay channel, either PET or SPECT technology can be employed to visualize the drug distribution. The most common devices for SPECT imaging are Anger cameras [1]. However, their low spatial resolution is suboptimal for preclinical studies on laboratory animals. Compton cameras could offer a solution, though their applicability is constrained by photon energy requirements – typically around 200 keV or higher – thus limiting the selection of isotopes and detectors suitable for this approach. The photon emitters most widely used in SPECT, such as ^{99m}Tc, ^{66}Ga, and ^{123}I, emit radiation in the 30 to 180 keV range. For this energy window, imaging tools with a

*Corresponding author e-mail address: rozhkov@jinr.ru

Received: 6 May 2025; Revised: 28 May 2025; Accepted: 29 May 2025; Published: 17 June 2025
Copyright: © by the author(s), 2025, under license to Joint Institute for Nuclear Research. This article is an open access article distributed under the terms and conditions of the Creative Commons Attribution-NonCommercial 4.0 International license (CC BY-NC License 4.0).

small field of view (FoV) are more appropriate. These are particularly well-suited for research involving small rodents. Their spatial resolution generally ranges from 0.2 to 2 mm and is strongly influenced by the collimator design. Pinhole collimators and their modifications are frequently applied [2]. Multi-pinhole configurations, in particular, offer improved sensitivity while preserving high spatial resolution.

This article presents the characteristics of a SPECT imaging system based on a Timepix detector with a CdTe sensor, using MURA-type coding apertures collimators.

2. The SPECT setup

The SPECT setup studied in this paper is based on the use of a hybrid pixel detector made of a Timepix readout chip, with a 2-mm-thick CdTe sensor. A MURA coding aperture with 31 rank basic pattern was used as a collimator [3].

The Timepix chips were developed by the Medipix collaboration at CERN [4]. Detectors based on them, in addition to recording the coordinates of the particle interaction in a sensor, are capable of measuring the energy released during the interaction. The Timepix chip can operate in several modes:

- Medipix — photon counting mode. In this mode, the chip counts how many times a signal exceeds a set threshold over a certain period of time.
- Time of arrival (ToA) — the chip measures when a signal exceeds a set threshold.
- Time over threshold (ToT) — the chip measures the signal duration over a certain threshold.

Since the signal duration over the threshold is proportional to the collected charge and thus to the energy deposited by the photon, the ToT mode allows us to determine the energy deposit in the sensor [5].

CdTe with a thickness of 2 mm was chosen as the sensor material, because CdTe has a higher absorption coefficient compared to Si and GaAs. The main advantages and disadvantages of this material are perfectly described in the review [6].

The detector area is 14.08 mm $\times$ 14.08 mm, which is significantly smaller compared to other gamma cameras. Therefore, the operation of the system for a small FoV must be ensured by a high-precision lensing system, which is provided by the coding aperture. In this work, we used a MURA-type coding aperture, with a matrix rank of 31 as a collimator. This type of collimator has a rectangular working area and, when rotated by 90 degrees, changes transparent elements to non-transparent ones and vice versa. This feature allows us to increase the signal-to-noise ratio [7]. The collimator, 1 mm thick, was made of tungsten, and the radius of holes was 170 μm.

Given the relatively small detector area, the basic mask pattern must fit entirely within the active sensor region. A rank-31 matrix provides a balance between spatial resolution and practical constraints, offering sufficient detail while maintaining a manageable number of elements. The element size and hole diameter were chosen as a compromise between desired resolution and the manufacturing capabilities available for producing well-defined apertures. This rank also ensures good mask transparency, robustness to decoding artifacts, and symmetry properties that simplify rotation and decoding operations [7].

The placement of the detector and the coding aperture is done by a duralumin mount, which allows adjusting the distance between them. The mount features a rotating platform, allowing quick rotation of the mask pattern by 90 degrees.

By changing the distance between the collimator and the detector, it is possible to change the FoV of the SPECT system:

$$\mathrm{FoV} = \frac{(f+d)(M-D)}{d} + D, \tag{1}$$

where FoV — FoV size, f — distance from the source to the collimator, d — distance from the collimator to the detector, M — the collimator size, D — the detector size.

In this work, the distance between the detector, the collimator, and the object under study was selected so that the FoV was 57.75 mm × 57.75 mm (Figure 1).

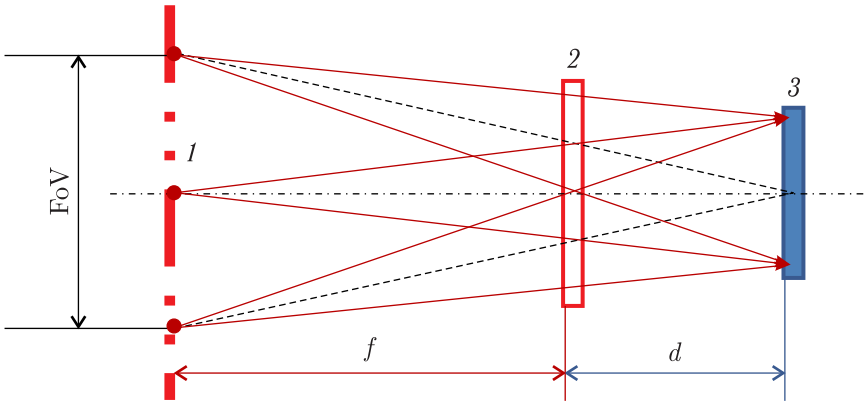

Figure 1. Layout of the SPECT setup: *1* — source plane, *2* — coding aperture, *3* — detector, FoV — field of view, f — distance from the source to the coding aperture, d — distance from the coding aperture to the detector.

The object was mounted on a dedicated rotating platform, allowing it to be turned around a single axis during imaging. This simplified the design of the experimental setup for phantom testing by eliminating the need for a rotating gantry. For SPECT characterization, 120 projections were acquired at different angular positions of the object.

3. Data preprocessing

Energy measurements in this study were conducted using the ToT mode of the Timepix chip. A pixel-by-pixel calibration was performed to convert the duration of signals over the threshold into a photon energy [5], with a bias voltage of –450 V and an energy threshold of 6 keV.

The energy threshold of 6 keV was selected based on the operating characteristics of the Timepix chip coupled with a 2-mm CdTe sensor. At this threshold, electronic noise and dark current contributions, especially prominent near the sensor edges, are effectively suppressed [4]. Tests with lower thresholds (3–4 keV) resulted in a significant increase in spurious hits and false clusters, leading to degradation of cluster-based energy measurements and increased uncertainty in event reconstruction.

Data from the Timepix detector were collected using the FitPix interface module [8]. The output data contained frames recording the coordinates of activated pixels and their energy deposition in ToT units. Neighboring activated pixels were grouped into clusters for further analysis.

Each aperture hole effectively operates as a pinhole collimator, creating a composite shadowgram that must be decoded to form the final image. The decoding step involves convolving the shadowgram with a decoding function [7]. However, because of the detector's pixelated

architecture and charge-sharing effects stemming from the 2-mm-thick CdTe sensor, data preprocessing is required. To address these challenges, specialized software was developed to process each frame, following these steps:

1. Selection of events based on cluster size.
2. Pixel-by-pixel energy calibration.
3. Filtering of events based on photon energy.
4. Reconstruction of photon interaction coordinates.
5. Decoding of the shadowgram.

Several factors determine the cluster size for photons with the energy up to 140 keV, including the diffusion of charge carriers during their drift to the readout electrodes, the fluorescent photons (whose free path in CdTe is up to 100 μm [9], which is comparable in size with almost two Timepix pixels), and the Compton electrons. Additionally, at high fluxes or with a long acquisition time, signals from several photons can overlap, forming larger clusters. The bias voltage applied to the sensor, which governs the drift time of the charge carriers and the acquisition time, also indirectly affects the cluster size.

Selecting an optimal acquisition time involves balancing the overlap of signals and the dead time due to frame readout. Overlapping signals can distort cluster formation and degrade projection quality, while shorter acquisitions, whilst reducing overlap, increase dead time, which is particularly undesirable with short-lived isotopes. Figure 2 shows how the number of registered clusters depends on acquisition time per frame during a total measurement of one minute. Longer acquisition time leads to more registered events because of reduced dead time. However, when acquisition time goes above 0.1 s, the number of registered events decreases substantially due to increased overlaps forming larger clusters. Consequently, an acquisition time of 0.1 s was selected as optimal, yielding the highest number of events with minimal overlap.

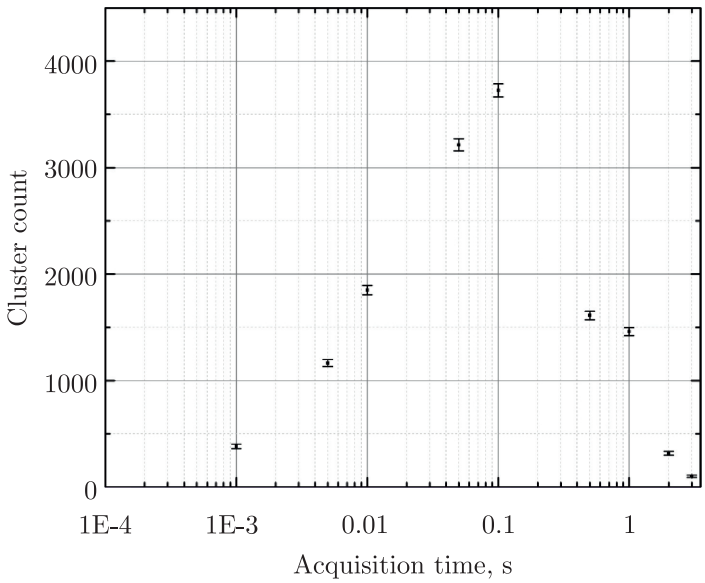

Figure 2. Dependence of the cluster count on the acquisition time.

The dependence of detection efficiency and reconstructed energy for photons from the decay of ^{99m}Tc indicates that the charge collection efficiency in a 2-mm-thick CdTe sensor stabilizes at bias voltages above –400 V, approaching the asymptotic value by less than 7%. Furthermore, the per-pixel energy calibration conducted at a bias voltage of –450 V remains applicable at higher voltages with an uncertainty less than 1% (Figure 3).

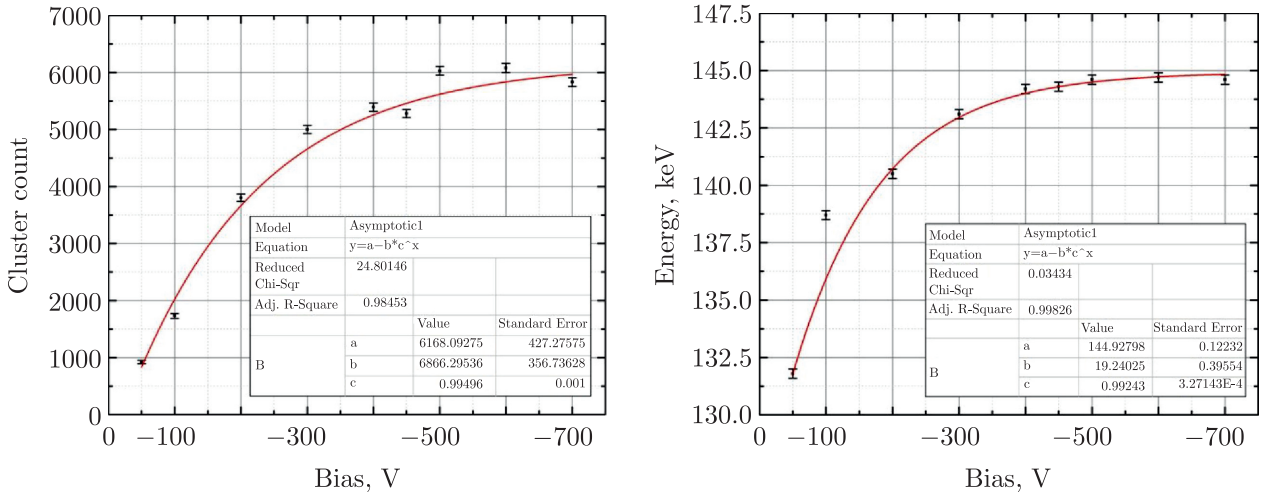

Figure 3. Dependency of the registered cluster count (left) and cluster energy (right), versus the bias voltage on the sensor.

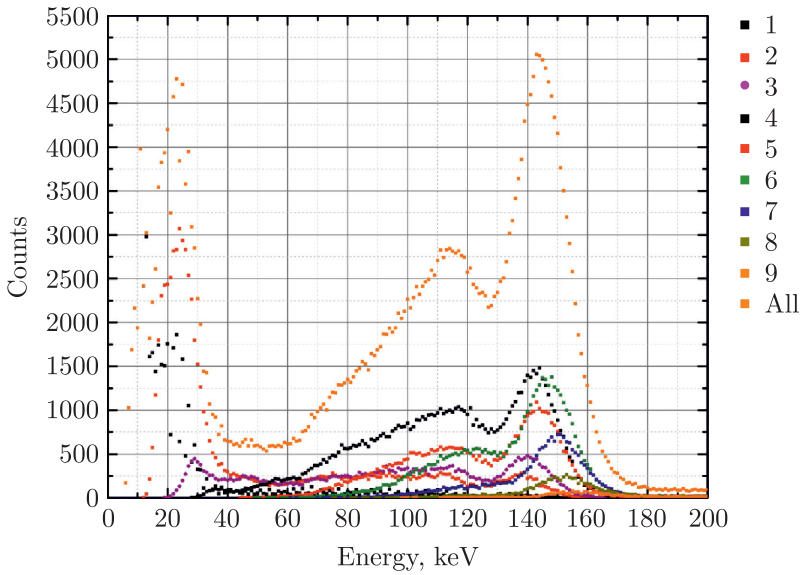

Figure 4. ^{99m}Tc energy spectra for various cluster size.

A small discrepancy is clearly visible between the measured energy (145 keV) and the photopeak energy of ^{99m}Tc (140.5 keV) in Figure 4. This discrepancy is caused by the energy miscalibration for many-pixel clusters, since the existing calibration relies solely on single-pixel clusters. The maximum energy that was used for calibration was 70 keV. The induced charge on some pixels remains below the threshold and thus goes undetected, particularly at photon energy above 30 keV. Consequently, the reference energy used for calibration is defined by single-pixel clusters whose recorded charge is lower than the actual charge generated during the interaction of photons with the sensor. As the cluster size increases, the discrepancy also increases, since this small fraction of the charge is not visible.

Larger clusters contribute less to the ^{99m}Tc photopeak and more to the "tails" of the energy spectrum. These tails arise from the overlap of events in smaller clusters, encompassing clusters larger than nine pixels. Single-pixel and two-pixel clusters primarily represent fluorescent photons, but unlike two-pixel clusters, single-pixel clusters do not contribute to the ^{99m}Tc photopeak.

To identify ^{99m}Tc photons, clusters with the reconstructed energy within 22% off the photopeak were selected, corresponding to the energy resolution of Timepix detector (at 140 keV). Clusters spanning 2–9 pixels can be 110–220 μm in size, which substantially deteriorates the spatial resolution of the reconstructed images. To mitigate this issue, the cluster's total charge is reassigned to the pixel with the highest recorded energy. Thus, before the image decoding, the data are converted into a two-dimensional array of single-pixel events with energies around the ^{99m}Tc photopeak region.

4. System tests

The methods of measuring the main characteristics of the system, such as contrast, sensitivity, uniformity, linearity, SNR, spatial resolution, energy resolution, etc., as well as the detector data preprocessing algorithm and clustering, and the methods for improving SNR using machine learning, have been published elsewhere [10–12]. This paper presents results on basic tests developed following the IAEA recommendations and relevant documents of national standard agencies [13–16]. The reconstructed projections were not subjected to any additional filtering, except for cluster preprocessing described above.

4.1. Uniformity

Intrinsic uniformity provides a quantitative measure of potential artifacts within the FoV. To determine this parameter, a pointlike source is often used. In our case, an X-ray tube with a 75-μm focal spot was used[1], and the exposure time was set to 5 min. The analysis of the results is carried out in the central field of the detector, highlighted in red. This was done to avoid taking into account the influence of edge effects such as leakage currents, which can make a significant contribution to the homogeneity measurement (Figure 5).

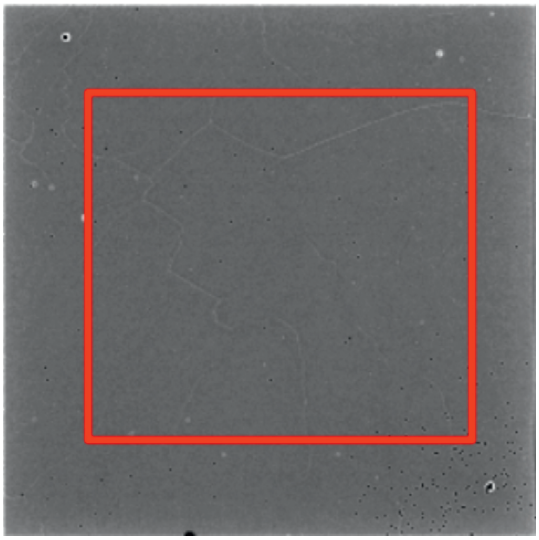

Figure 5. Reconstructed image of the detector response to an X-ray source.

In addition to intrinsic uniformity, both integral and differential system uniformities were determined. A flood phantom with the dimensions 45 × 50 × 5 mm^3 was used, positioned to cover as much of the 57 mm × 57 mm FoV as possible (Figure 6). The detector regions used to

[1]SB 120-350 by Source Ray Inc.

determine intrinsic uniformity were selected for integral uniformity measurement, corresponding to the flood phantom's placement. Figure 7 shows an image of distributed sources from a flood phantom, the total activity of the ^{99m}Tc solution in the phantom was 1 MBq. Given the low activity, a 2×2 binning was applied to the decoded image to increase the statistics in each pixel.

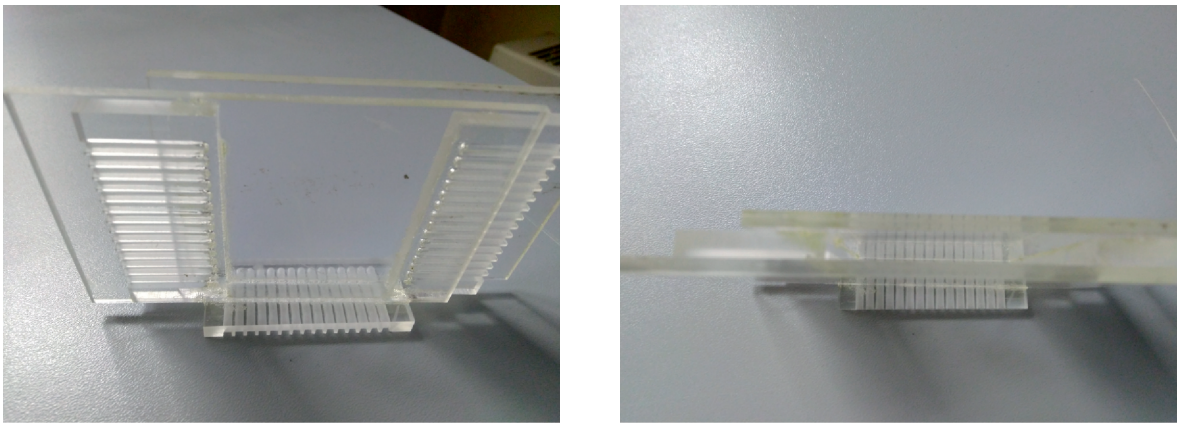

Figure 6. Flood phantom: side view (left), top view (right).

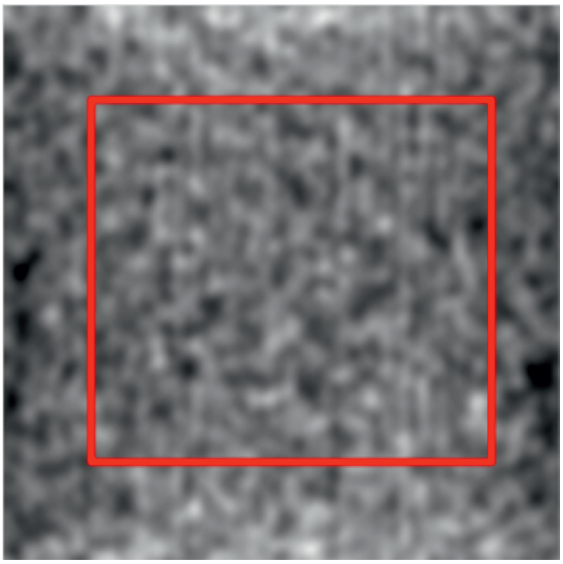

Figure 7. Reconstructed image of a flood phantom.

Before assessing uniformity, any pixel whose count is below 75% of the average number of pulses is set to zero. The non-zero pixels are then smoothed over nine points with the following weights:

$$\begin{array}{ccc} 1 & 2 & 1 \\ 2 & 4 & 2 \\ 1 & 2 & 1. \end{array}$$

These weights are a discrete approximation of a two-dimensional Gaussian filter ($\sigma \approx 1$). This filtering method is well-established in the literature [13–16] and is frequently applied prior to uniformity evaluation. It suppresses pixel-level noise while preserving spatial structures, thus improving the reliability of the uniformity measurement.

To calculate the integral uniformity, the following formula was used:

$$\text{integral uniformity} = \frac{\max - \min}{\max + \min}, \tag{2}$$

where max is the maximum value of the total number of photons registered by the detector and min is the minimum one [17]. The integral uniformity was calculated only for the area covered by the phantom image, neglecting narrow side bands of FoV.

Differential uniformity was also calculated using Eq. 2, over all possible (5×5 pixel) windows along horizontal and vertical directions, and the maximum value. This approach highlights the worst-case deviation in uniformity and is consistent with standard quality assurance practice [15, 16].

Thus, the integral and differential uniformity was determined for the same sensor area. The intrinsic uniformity is 92%. Integral uniformity and differential uniformity are 44% and 84%, respectively.

The low integral uniformity partially comes from the presence of artifacts caused by the shortcomings of the shadowgram reconstruction. The reconstruction algorithm currently does not take into account the circular shape of the collimator holes, assuming it to be square. The use of filters and the development of more advanced reconstruction methods can significantly reduce the number of artifacts and increase the system integral uniformity.

By changing the position of the studied area within the FoV, a certain error in estimating the integral and differential heterogeneity was determined, which does not exceed 0.5%.

In the current implementation of the reconstruction algorithm, the shape of the apertures was approximated by square holes. This simplified model reduces computational cost, but it may indeed affect the spatial characteristics of the reconstructed image.

To quantitatively assess the distortion, we calculated the normalized root mean square error (NRMSE) between the point spread functions (PSFs) obtained using square and circular apertures:

$$\text{NRMSE} = \frac{\sqrt{\sum_i (A_i - B_i)^2}}{\max(B)}, \tag{3}$$

where A_i and B_i are the pixel values of the PSF generated for square and circular apertures, respectively. NRMSE values greater than 0.1 indicate noticeable divergence and potential influence on reconstruction artifacts (Figure 8).

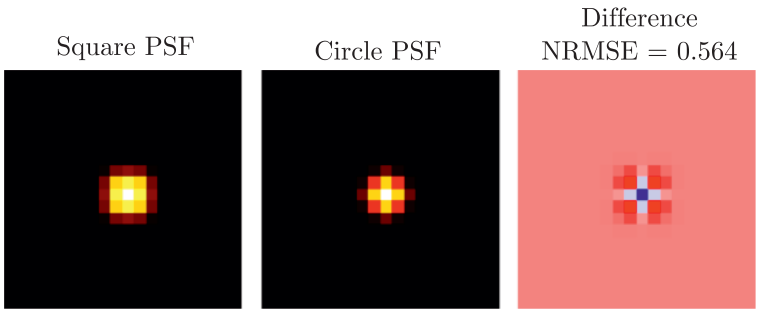

Figure 8. Difference between the point spread functions (PSFs) obtained using square and circular apertures.

In practice, this approximation leads to a broadening of the PSF profile, degradation of spatial resolution (increase in FWHM, Full Width at Half Maximum), and decreased background uniformity when reconstructing homogeneous regions.

NRMSE is only one possible metric for assessing the impact of geometric simplifications. Alternative approaches include:

- measurement of the FWHM of the PSF profile along the central axis;
- analysis of the uniformity index in homogeneous regions;
- estimation of artifact power by comparing reconstructed and model images;
- calculation of PSF centroid shift [18].

Approximating the aperture shape affects the accuracy of PSF modeling and, consequently, the reconstruction characteristics, particularly uniformity and artifact level. In this study, a preliminary quantitative assessment of this influence was carried out using NRMSE.

4.2. Linearity

The linearity is the measure of geometry distortion of source distribution by the SPECT system in the object under study. Measuring linearity is especially important for SPECT systems equipped with scintillation detectors; because of them, the linearity will be affected by the inhomogeneity and defects of the crystal, as well as by the accuracy of the placement of PMTs. A linearity of 100 percent indicates that the reconstructed image does not distort the relative position of sources.

To determine the linearity, a phantom was used with capillaries aligned parallel in a row. The body of the phantom was made of plexiglass with a mechanical precision of 0.05 mm (Figure 9). Inside the phantom, there were 11 capillaries, each 1.1 mm in diameter. The distance between the centers of the capillaries was 2 mm, and each capillary was 20 mm long. The rotation axis of the phantom passed through the central capillary. All even capillaries were filled with ^{99m}Tc solution. The total activity was in 83 MBq. For the tomographic reconstruction, projection images were taken with an exposure time of 2 min per projection.

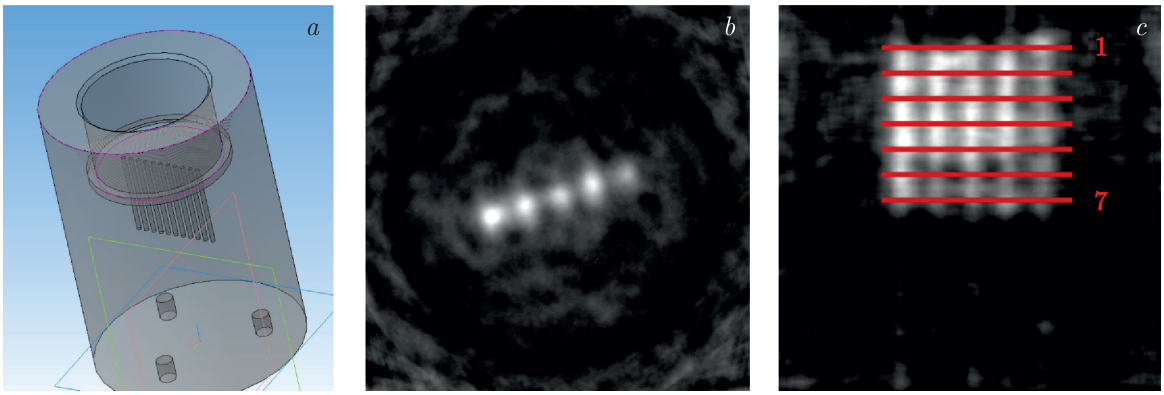

Figure 9. Linearity phantom: *a*) drawing; *b*) reconstructed slice; *c*) sagittal section. Lines correspond to measured profiles.

After the reconstruction, a sagittal section was selected that passed through the centers of each of the capillaries (Figure 10). On this section, seven profiles were constructed passing through each capillary along the entire height of the phantom. The location of the intensity maximum, corresponding to the center of each capillary, was determined along each profile. Subsequently, these data were compared with the phantom's blueprint to determine the deviation of the measured center from its actual value. The deviations were less than 0.2 mm on a 20 mm length of the capillary, or, in other words, less than 1%. Such a high accuracy is ensured by the high precision of the collimator pattern manufacture, 0.001 mm, as well as the high precision of the pixel matrix placement of the detector.

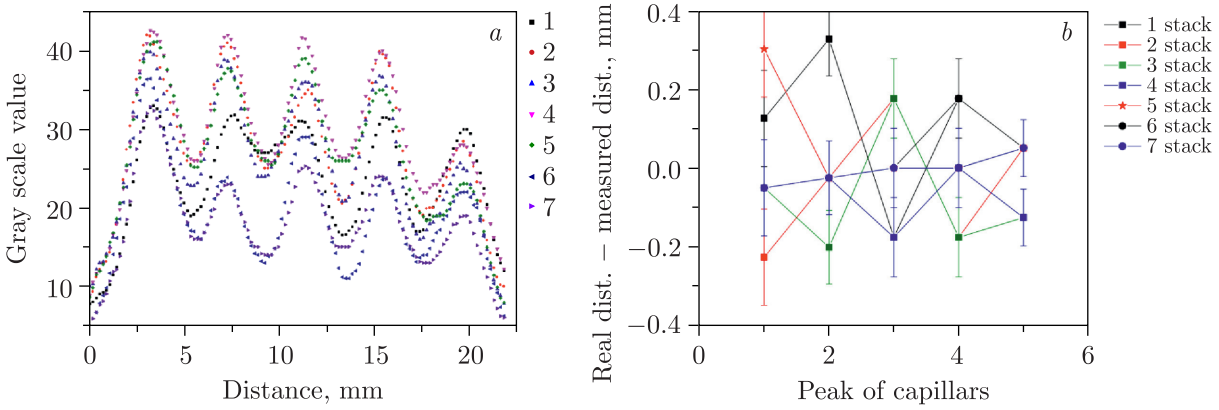

Figure 10. *a*) Capillary plot profiles measured by linearity phantom; *b*) peak position in section.

The data for the triplets of linearity phantom slices are presented in Figure 11.

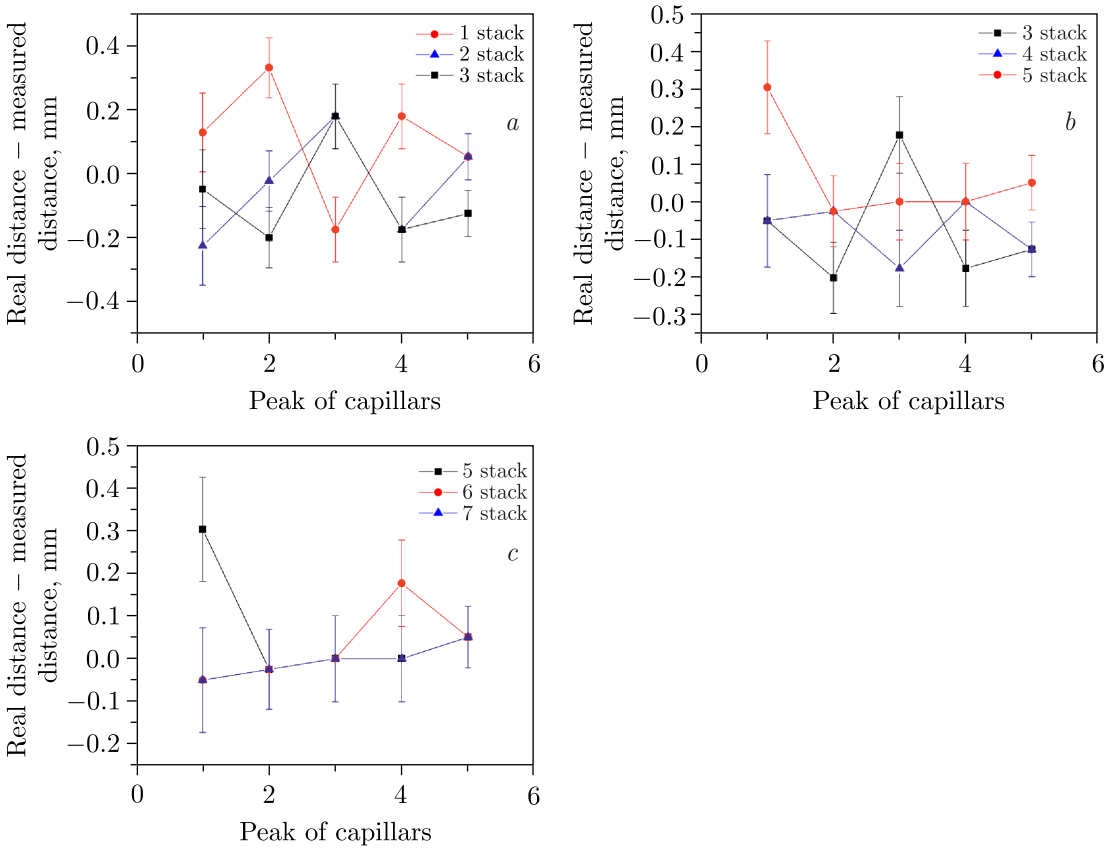

Figure 11. Linearity phantom profiles: *a*) 1–3 slices; *b*) 3–5 slices; *c*) 5–7 slices.

4.3. Spatial resolution

Unlike the initial system tests conducted with a FoV of 30 mm × 30 mm for planar images [10], this series of experiments was aimed at the study of tomographic spatial resolution and involved 3D reconstruction of distributed sources for a FoV of 57.75 mm × 57.75 mm. Due to the pixel structure of the sensor, the increase in the FoV causes the spatial resolution to decrease proportionally.

The following phantom was used to measure spatial resolution. The central capillary's axis passed through the phantom's rotation axis. At an equal distance from the central capillary, two other capillaries were aligned parallel, so that their centers formed an isosceles right triangle. The diameter of each capillary was 1.1 mm (Figure 12).

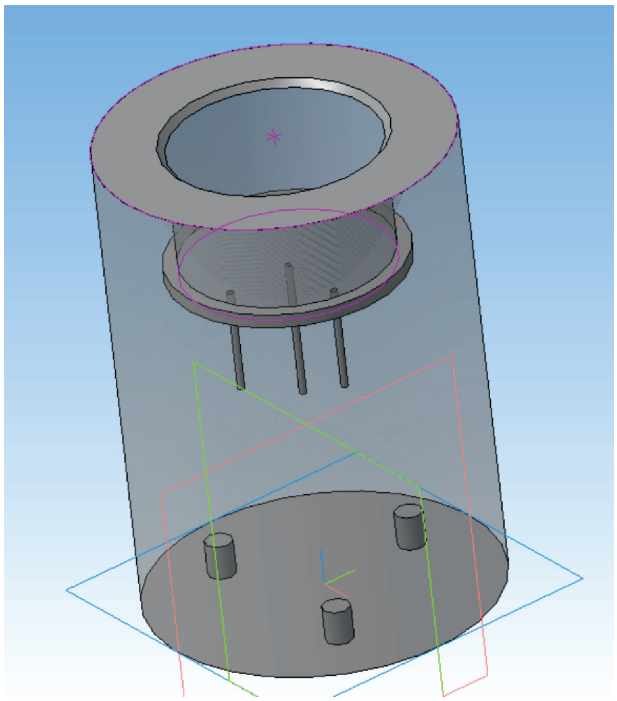

Figure 12. Scheme of the phantom for measuring spatial resolution.

From Figure 13, it can be seen that capillaries with sources are hardly distinguishable on the projection. However, even such projections allow satisfactory tomographic reconstruction of distributed sources.

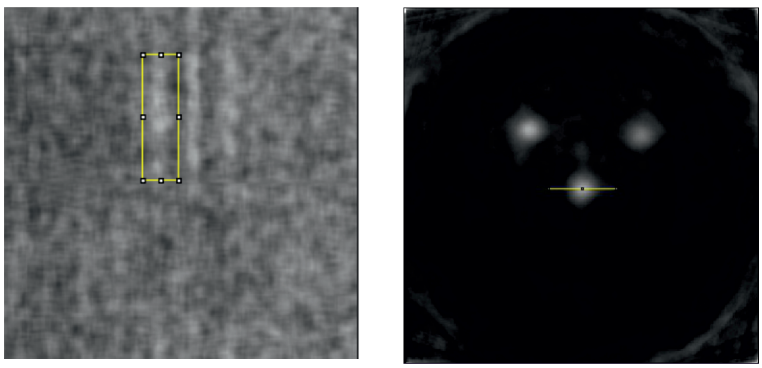

Figure 13. Original projections (left) and slice (right) of the phantom data.

The degradation of the SNR is caused by sources located behind and in front of the focal plane [19]. To improve the quality of projection data, filtration can be applied or, as shown in [20], machine learning methods can be used to improve significantly the SNR. For projections filtered by the CED-line algorithm, the FWHM of the capillary profile is shown to be consistent with the size of the capillary (Figure 14).

To determine the tomographic spatial resolution (FWHM), the capillary profile in the reconstructed slice was fitted by the convolution of a rectangular function and a Gaussian function.

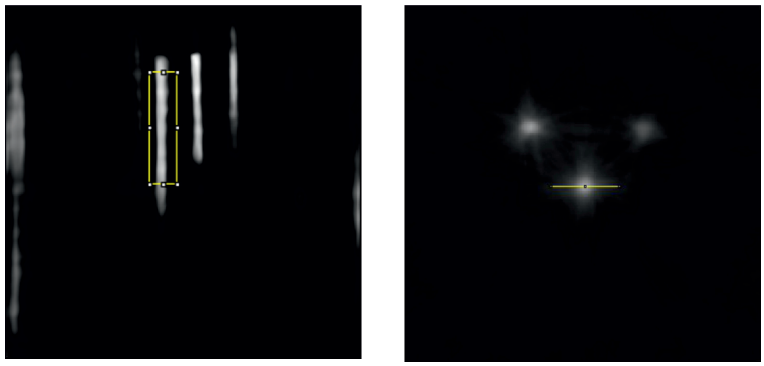

Figure 14. Projections (left) and slices (right) of the phantom data filtered using the CED algorithm.

The width of the rectangular function was fixed to be 1.1 mm, which is the diameter of the capillary. The parameter σ of the Gaussian function was free and fitted to determine the resolution. The result is shown in Figure 15 for original profile and after applying the CED algorithm. The spatial resolution is 3.0 mm for the original profile, and it improves up to 2.0 mm after filtration (Figure 16), which is consistent with our previous results obtained in 2D geometry.

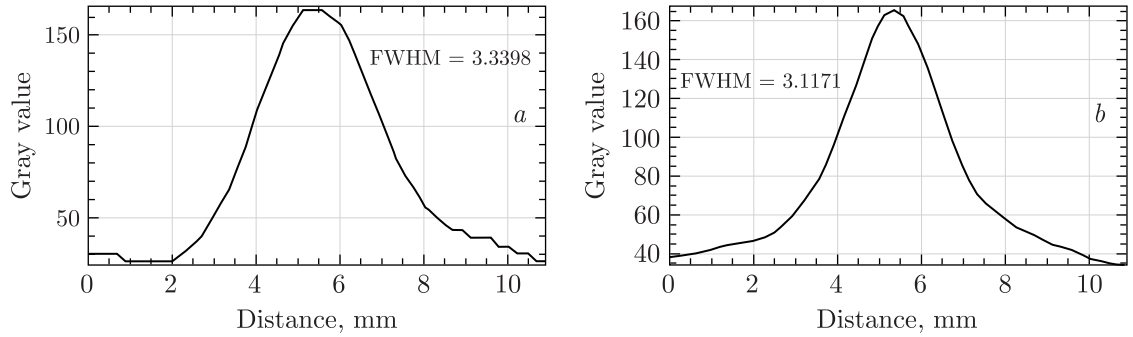

Figure 15. Original capillary plot profile (a) and capillary plot profile after CED algorithm (b).

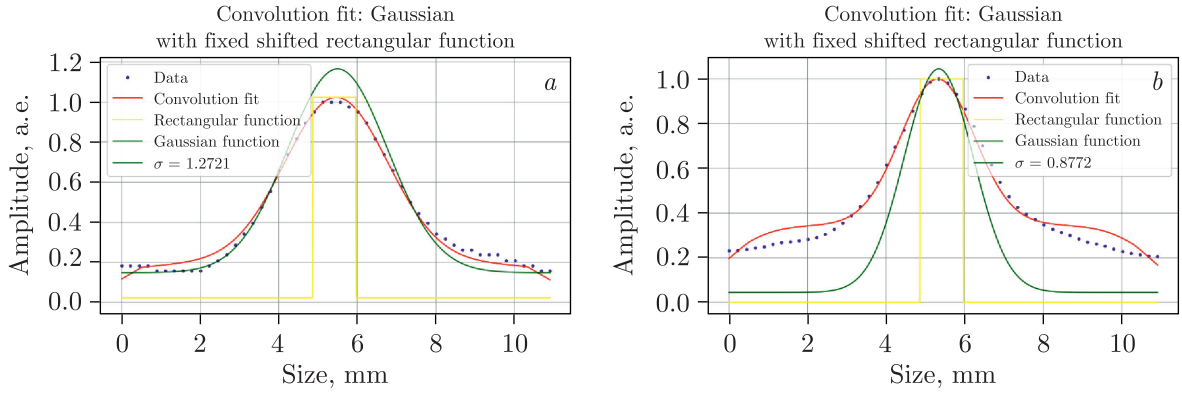

Figure 16. Capillary profile without filtering (a) and after CED-algorithm filtration (b).

The inaccuracy of spatial resolution measurement can vary within one pixel and is ± 0.23 mm. This is due to the fact that a pixel detector is used. When recalculating this, it becomes clear that one pixel hides the integral information of sources located on an area of 0.23 mm $\times$ 0.23 mm.

4.4. Contrast

To evaluate the contrast of the SPECT system, a phantom consisting of two identical cells equidistant from the center of rotation was used (Figure 17). The distance between cell centers was 10 mm. The total activity introduced into the phantom was 75 MBq. The cells were filled up with the solutions of 40% and 60% of the total activity, respectively. After reconstruction, the stack of slices was summed, and the intensity for the two cells were determined from the resulting profile. The ratio of the cell intensity was equal 0.67, closely matching the activity placed into the cells (Figure 18), which was 0.68 ± 0.01. Uncertainty was combined with activity device measurements. Thus, the contrast of the system is sufficiently high and accurate, making the system suitable for quantitative imaging.

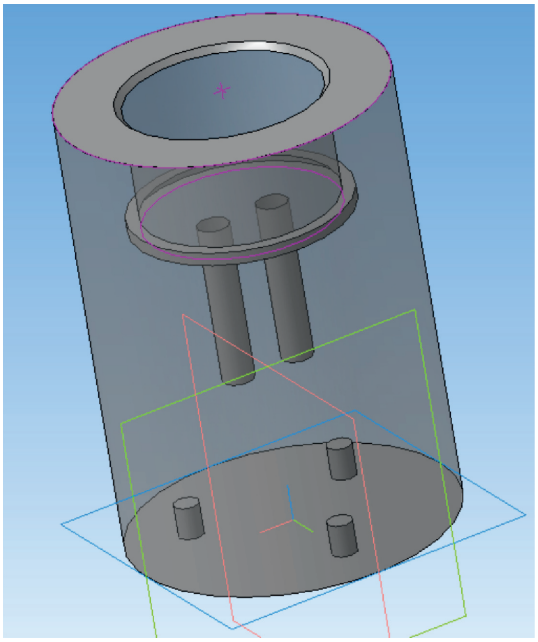

Figure 17. Phantom used for contrast evaluation.

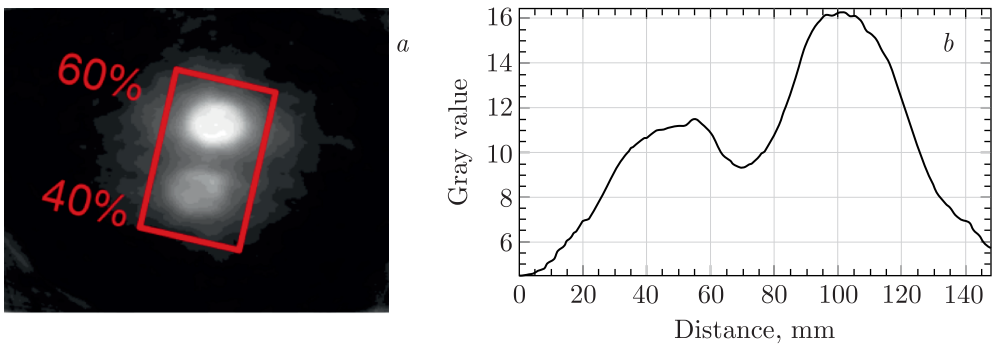

Figure 18. Contrast phantom slice (a), contrast phantom profile (b).

4.5. Sensitivity

Sensitivity is defined as the ratio of the number of photons registered by the system to the number of photons emitted within a solid angle covered by the detector. The sensitivity can be estimated for a sample without a collimator (intrinsic sensitivity) and with the collimator (system sensitivity).

The 2-mm diameter capillary-shaped ^{99m}Tc source with an activity of 100 MBq was located at a distance of 215 mm from the collimator. System sensitivity can be estimated using the formula

$$S = \varepsilon_{\text{geom}} \cdot \varepsilon_{\text{att}} \cdot \varepsilon_{\text{det}} \cdot f_{\text{col}} \cdot A, \tag{4}$$

where S — system sensitivity, [cps/MBq], $\varepsilon_{\text{geom}}$ — geometric efficiency (the solid angle covered by the detector), ε_{att} — attenuation factor in air (Eq. 5), ε_{det} — detection efficiency (including absorption in the crystal and other losses), f_{col} — collimator efficiency (fraction of photons passing through collimator holes without scattering), A — source activity, [MBq].

$$\varepsilon_{\text{att}} = e^{-\mu_{\text{air}} \cdot x}, \tag{5}$$

where μ_{air} is the linear attenuation coefficient of air, and x is the distance to the source.

The decrease in the activity caused by the source decay is not taken into account in the calculations since the acquisition time (10 s) is significantly less than the half-life of ^{99m}Tc (362 min).

The system sensitivity calculated by formula 4 is equal to 79 cps/MBq ±3.5 cps/MBq, based on repeated measurements and count statistics. However, the total efficiency in 4π solid angle, largely determined by a small detector surface (the solid angle covered by the detector is 0.0043 sr), is only 0.034%. Also, 0.25% of photons are lost due to absorption in the air. The factors influencing the system efficiency include the detection efficiency of the detector and the collimator geometry. The collimator geometry allows passing through as much as 39% of incoming particles. In turn, the detection efficiency of photons with an energy of 140 keV is 60% for a 2-mm-thick CdTe sensor.

5. Ways to improve the spatial resolution of the system

Our prototype system on Timepix + CdTe demonstrated a tomographic spatial resolution of about 3 mm (FWHM) on a FoV of 57 mm × 57 mm. With advanced data processing, we were able to improve the resolution to 2 mm. However, this is significantly worse than the sub-millimeter resolution of commercial systems. The main reasons for the 2–3 mm limitation in our case and the differences from industrial scanners are as follows:

- The current resolution of our imaging system reflects a trade-off between a large FoV and relatively high detail in the developed phantoms. Achieving a resolution of 0.5–1 mm will require narrowing the FoV.
- Improving spatial resolution requires substantial optimization and enhancement of reconstruction algorithms.
- Enhancing spatial resolution requires accurate representation of hole geometry and reduction of their diameter.
- Introducing iterative reconstruction with a complete system model is a key step toward achieving high spatial resolution.
- A balance must be found between spatial resolution and detection efficiency. The simultaneous use of multiple detector heads would increase system cost, but may offer a viable solution to this challenge.

6. Conclusion

The results of this study demonstrate the feasibility of creating a compact SPECT system based on the Timepix detector with a 2-mm-thick CdTe sensor and a MURA-type coded aperture. The tests and experiments conducted included assessing the system's uniformity, linearity,

spatial resolution, and contrast, as well as comparing performance under various filtering and reconstruction approaches.

1. We evaluated intrinsic, integral, and differential uniformity, equal to 92%, 44% and 84%, respectively. The integral uniformity metrics can be further improved by using better shadowgram reconstruction algorithm.

2. Measurements of linearity using a capillary phantom confirmed the absence of significant distortions in the reconstructed images, indicating high accuracy in coordinate determination.

3. Spatial resolution (FWHM) was determined to be 3.0 mm for the FoV of 57 mm × 57 mm. More advanced data processing and decoding demonstrated the potential to achieve a spatial resolution of about 2.0 mm.

4. Experiments with a "hot" phantom (different amount of the radiotracer in equal volumes) confirmed that the system can distinguish areas with varying activity levels, closely matching the theoretical ratio. It indicates a high contrast of the system.

5. The system's overall sensitivity is primarily limited by the small detector area and certain design features of the collimator.

The results obtained confirm the suitability of the prototype SPECT system for conducting preclinical experiments in a small FoV using ^{99m}Tc-based radiopharmaceuticals. Possible improvements in reconstruction methods, the use of machine learning algorithms for data processing, and further optimization of collimator and transducer geometry can significantly improve image quality.

Author contributions

V. Rozhkov: Conceptualization, Methodology, Software, Original draft preparation, Visualization, Investigation; I. Hernández Coauthor: Data curation, Writing, Reviewing and Editing; A. Leyva: Validation, Writing, Reviewing and Editing; A. Zhemchugov: Supervision, Writing, Reviewing and Editing.

Conflicts of Interest

The authors declare no conflicts of interest.

References

[1] H. O. Anger, Scintillation camera, Rev. Sci. Instrum. 29 (1958) 27–33. doi: https://doi.org/10.1063/1.1715998.

[2] MILabs, Revolutionary new pinhole technology allows simultaneous high-resolution *in vivo* SPECT and PET, 2018, https://www.milabs.com/milabs-announces-revolutionary-new-pinhole-technology-allows-simultaneous-high-resolution-in-vivo-spect-and-pet/.

[3] M. J. Cieslak, K. A. A. Gamage, R. Glover, Coded-aperture imaging systems: Past, present and future development — A review, Radiat. Meas. 92 (2016) 59–71. doi: https://doi.org/10.1016/j.radmeas.2016.08.002.

[4] X. Llopart, R. Ballabriga, M. Campbell, L. Tlustos, W. Wong, Timepix, A 65k programmable pixel readout chip for arrival time, energy and/or photon counting measurements, Nucl. Instrum. Meth. A 581 (2007) 485. doi: https://doi.org/10.1016/j.nima.2007.08.079.

[5] A. P. Butler, P. H. Butler, S. T. Bell et al., Measurement of the energy resolution and calibration of hybrid pixel detectors with GaAs:Cr sensor and Timepix readout chip, Phys. Part. Nucl. Lett. 12 (2015) 97.

[6] S. Abbaspour, B. Mahmoudian, J. P. Islamian, Cadmium telluride semiconductor detector for improved spatial and energy resolution radioisotopic imaging, World J. Nucl. Med. 16 (2017) 101–107. doi: https://doi.org/10.4103/1450-1147.203079.

[7] S. R. Gottesman, E. E. Fenimore, New family of binary arrays for coded aperture imaging, Appl. Opt. 28 (1989) 4344–4352. doi: https://doi.org/10.1364/AO.28.004344.

[8] V. Kraus, M. Holik, J. Jakubek et al., FITPix — fast interface for Timepix pixel detectors, JINST 6 (2011) C01079. doi: https://doi.org/10.1088/1748-0221/6/01/C01079.

[9] L. Tlustos, Performance and limitations of high granularity single photon processing X-ray imaging detectors. Thesis, Technische Univ. Wien, Vienna, Austria, 2005, http://inis.iaea.org/search/search.aspx?orig_q=RN:38037565.

[10] V. Rozhkov et al. Visualization of radiotracers for SPECT imaging using a Timepix detector with a coded aperture, JINST 15 (2020) P06028. doi: https://doi.org/10.1088/1748-0221/15/06/P06028.

[11] V. Rozhkov, A. Zhemchugov, A. Leyva, P. Smolyansky, Uniformity and sensitivity measurements for small field of view pixelated SPECT system with coded aperture, Phys. Part. Nucl. Lett. 19 (2022) 594–596. doi: https://doi.org/10.1134/S1547477122050363.

[12] V. A. Rozhkov, A. S. Zhemchugov, A. Leyva, P. I. Smolyanskiy, 3D gamma source SPECT visualization using Timepix detectors and encoding apertures, Phys. At. Nucl. 85 (2022) 1501–1504. doi: https://doi.org/10.1134/S1063778822090319.

[13] International Atomic Energy Agency, Quality assurance for SPECT systems, IAEA Human Health Series, No. 6, Vienna, Austria (2009), p. 263.

[14] International Atomic Energy Agency, Planning a clinical PET center, IAEA Human Health Series, No. 11, Vienna, Austria (2010), p. 160.

[15] National Electrical Manufacturers Association (NEMA), NEMA NU 1-2018, 2018, https://www.techstreet.com/nema/standards/nema-nu-1-2018?product_id=2073744.

[16] National Electrical Manufacturers Association (NEMA), NEMA NU 2-2018, 2018, https://www.techstreet.com/nema/standards/nema-nu-2-2018?product_id=2017225.

[17] Md. R. Hasan, Md. H. R. Khan, Md. R. Rahman, Md. S. Parvez, Md. R. Islam, A. K. Paul, Quality control of gamma camera with SPECT systems, IJMPCERO, 6 (2017) 225–232. doi: 10.4236/ijmpcero.2017.63021.

[18] Lu Tianhuan et al., An accurate centroiding algorithm for PSF reconstruction, Astron. J., 156 (2018) 14. doi: 10.3847/1538-3881/aac5f7.

[19] G. A. Fedorov, S. A. Tereshchenko, Integrating encoding systems for recording ionizing radiation. Meas. Tech. 40 (1997) 164–174. doi: https://doi.org/10.1007/BF02504042.

[20] T. Meissner, V. Rozhkov, J. Hesser, W. Nahm, N. Loew, Quantitative comparison of planar coded aperture imaging reconstruction methods, JINST 18 (2023) P01006. doi: https://doi.org/10.1088/1748-0221/18/01/P01006.